Article

Recovery of Lithium from Industrial Li-Containing Wastewater Using Fluidized-Bed Homogeneous Granulation Technology

Van Giang Le [1], The Anh Luu [1], Huu Tuan Tran [2,3], Ngoc T. Bui [4], M. Mofijur [5,6], Minh Ky Nguyen [7], Xuan Thanh Bui [8], M. B. Bahari [9], Hoang Nhat Phong Vo [10], Chi Thanh Vu [11], Guo-Ping Chang Chien [12] and Yao-Hui Huang [13,*]

1 Central Institute for Natural Resources and Environmental Studies, Vietnam National University, Hanoi 100000, Vietnam; levangiangcres@vnu.edu.vn (V.G.L.); ltanh@cres.edu.vn (T.A.L.)
2 Laboratory of Ecology and Environmental Management, Science and Technology Advanced Institute, Van Lang University, Ho Chi Minh City 70000, Vietnam; tranhuutuan@vlu.edu.vn
3 Faculty of Applied Technology, School of Engineering and Technology, Van Lang University, Ho Chi Minh City 70000, Vietnam
4 School of Chemical, Biological, and Materials Engineering, University of Oklahoma, Norman, OK 73019, USA; ngoctbui21@ou.edu
5 Centre for Technology in Water and Wastewater, School of Civil and Environmental Engineering, University of Technology Sydney, Ultimo, NSW 2007, Australia; mdmofijur.rahman@uts.edu.au
6 Mechanical Engineering Department, Prince Mohammad Bin Fahd University, Al Khobar 31952, Saudi Arabia
7 Faculty of Environment and Natural Resources, Nong Lam University, Hamlet 6, Linh Trung Ward, Ho Chi Minh City 70000, Vietnam; nmky@hcmuaf.edu.vn
8 Faculty of Environment and Natural Resources, Ho Chi Minh City University of Technology, Ho Chi Minh City 70000, Vietnam; bxthanh@hcmut.edu.vn
9 Faculty of Science, Universiti Teknologi Malaysia, Johor Bahru 81310, Malaysia; mahadibahari@utm.my
10 Climate Change Cluster, Faculty of Science, University of Technology Sydney, 15 Broadway, Ultimo, NSW 2007, Australia; phong.vo@uts.edu.au
11 Civil and Environmental Engineering Department, The University of Alabama in Huntsville, Huntsville, AL 35899, USA; thaanhchivu@gmail.com
12 Center for Environmental Toxin and Emerging Contaminants Research, Cheng Shiu University, Kaohsiung 83347, Taiwan; guoping@gcloud.csu.edu.tw
13 Department of Chemical Engineering, National Cheng Kung University, Tainan 71710, Taiwan
* Correspondence: yhhuang@mail.ncku.edu.tw

Abstract: In this study, a novel fluidized-bed homogeneous granulation (FBHo-G) process was developed to recover lithium (Li) from industrial Li-impacted wastewater. Five important operational variables (i.e., temperatures, pH, $[P]_0/[Li]_0$ molar ratios, surface loadings, and up-flow velocities (U_{mf})) were selected to optimize the Li recovery (TR%) and granulation ratio (GR%) efficiencies of the process. The optimal operational conditions were determined as the following: a temperature of 75 °C, pH of 11.5, $[P]_0/[Li]_0$ of 0.5, surface loading of 2.5 kg/m^2·h, and U_{mf} of 35.7 m/h). The TR% and GR% at optimal condition could be as much as 90%. The material characterization of the recovery pellet products showed that they were highly crystallized Li_3PO_4 (purity ~88.2%). The pellets had a round shape and smooth surface with an average size of 0.65 mm, so could easily be stored and transported. The high purity enables them to be further directly reused as raw materials for a wide range of industrial applications (e.g., in the synthesis of cathode materials). Our calculation shows that the FBHo-G process could recover up to 0.1845 kg of lithium per cubic meter of Li-containing wastewater, at a recovery rate of ~90%. A brief technoeconomic analysis shows that FBHG process had economic viability, with an estimate production cost of USD 26/kg Li removed, while the potential gained profit for selling lithium phosphate pellets could be up to USD 48 per the same volume of wastewater and the net profit up to USD 22/m^3 Li treated. In all, fluidized-bed homogeneous granulation, a seedless one-step recovery process, opens a promising pathway toward a green and sustainable recycling industry for the recovery and application of the resource-limited lithium element from nonconventional water sources.

1. Introduction

Lithium is a non-renewable and highly market-valued metal that is an important input material for a wide range of industries (e.g., the pharmaceutical, metallurgical, electric vehicle, and renewable energy storage industries) [1–3]. For example, lithium phosphate (Li_3PO_4) is used for manufacturing lithium metal and other secondary Li products [4–6]. Lithium phosphate is known for exhibiting high thermal stability, making it suitable for use in high-temperature processes that are often involved in the preparation of advanced lithium-ion battery materials [7,8]. This stability ensures that it can withstand the harsh conditions required for the synthesis of electrode materials. Lithium phosphate can be used as an electrolyte additive to enhance the safety and stability of the battery. It helps prevent issues like thermal runaway and dendrite formation, which can lead to battery failure or even safety hazards [4,9]. The presence of phosphorus in lithium phosphate can be beneficial for the structural stability of electrode materials [10]. Phosphorus can help mitigate volume changes that occur during charge and discharge cycles, reducing the risk of electrode cracking and capacity fade [11,12].

However, global crude Li production will be diminishing, making it a limited product in the near future [13]. It is estimated that 11 million tons of spent LIBs will be discarded by 2030 [14], of which less than 5% will be treated and reused [15]. Spent LIB anodes that are not properly treated may also release toxic heavy metals and organic contaminants into the natural environment [15]. Therefore, Li recovery from salt lake brine [16] and spent LIB [17] wastewater remains a "hot" topic of sustainable chemical engineering.

In the market, several metal removal or recovery technologies have been developed to deal with the problem, e.g., leaching [18], solvent extraction [19,20], adsorption [21–25], electrocoagulation [26,27], nanofiltration [28,29], and chemical deposition [30,31]. Adsorption is proven as an effective technology for the removal of metal ions contamination in the water by applying electrostatic force, surface complexation, or Van der Waals force between the active surface of the adsorbent and the solute properties. Ding et al., reported that a manganese–titanium mixed ion sieve successfully adsorbs lithium ions at pH 12 and with 1.0 g/L of adsorbents to obtain a recovery efficiency of 81.42% within 600 min of contact time [16]. Recently, the application of advanced materials, such as nanoparticles, has attracted much attention. Various materials, such as hybrid biochar supported transition metal doped MnO_2 composites, H_2TiO_3, carbon nanotubes, and metal–organic frameworks, have been reported to be applied as adsorbents. However, the high production cost and the poor recovery of nanoparticles would be the disadvantages [32]. Moreover, a high lithium loading leads to rapid saturation of the adsorbent and increases the cost of adsorbent regeneration [33]. The recovery of lithium as Li_2CO_3 by chemical precipitation from Uyuni salar brine wastewater from the aluminum anode industry was reported by Álvarez-Ayuso et al. [34]. Wei et al., in 2005, applied the selective precipitation to produce purified Li_2CO_3 from dilute Li-rich brine to increase the practical value of Li-rich brine that is obtained using the conventional treatment method. Na_2CO_3 precipitation requires a pH of pH 9.0–10.0, which gives an Li removal efficiency of 40%, and the purity of precipitated Na_2CO_3 compounds is 20% [35]. The process produces a large amount of sludge, so the conventional chemical precipitation method is not suitable [36]. The disposal cost for the high-moisture sludge can account for up to 30% of the total process cost [37–40]. Fluidized-bed crystallization (FBC) is a cost-effective alternative, using fewer chemicals to produce low-water-content granulated particles (<5%), reducing sludge disposal costs by up to 79% compared to conventional methods. However, the heterogeneous support in FBC products can lead to impurity that would affect the recyclability of the reclaimed product [41–43].

The fluidized-bed granulation (FBG) has recently emerged as an advanced metal recovery technology, since it has shown high efficiencies for many metals and the products have a very low moisture content [44–46]. The FBG technologies include the fluidized-bed homogeneous granulation and the fluidized-bed heterogeneous granulation (FBHe-G). The FBHe-G shows some technical advantages compared to FBHoG, given that it requires fewer chemicals and produces particle products with a lower water content [47,48]. However, the products of the FBHe-G process are often of low purity due to the use of seeding materials (often silica) [49]. The FBHo-G, instead, was continuously improved to increase the product quality by using no seeding operational method [50–52].

This study aims to recover Li (in form of Li_3PO_4) from industrial Li-impacted wastewater using the FBHo-G process. The objectives are to (i) optimize the reaction temperatures, pH, $[P]_0/[Li]_0$ molar ratios, hydraulic retention times (HRTs), Li^+ initial concentrations, surface loadings, and up-flow velocities (U_{mf}); (ii) investigate the mechanisms of Li recovery; and (iii) study the physical size and surface chemical composition of the Li pellet products.

2. Materials and Methods

2.1. Industrially Li-Containing Wastewater and Chemicals

The raw Li-containing wastewater was obtained from a local mining company in Tainan City, Taiwan. The wastewater was stored in high-density polyethene bottles at 4 °C. Before use, the wastewater was filtered with a 0.45 μm membrane filters (Whatman, TISCH Scientific, Ohio, OH, USA) in order to remove suspended solids. The characteristics of the filtered Li-containing wastewater are shown in Table 1. Experiments were conducted within 8 h after receiving the wastewater. Lithium nitrate ($LiNO_3$, ≥98%) and sodium dihydrogen phosphate (Na_2HPO_4, ≥99%) were obtained from Sigma-Aldrich, Darmstadt, Germany. Sodium hydroxide (NaOH, ≥98%) and nitric acid (HNO_3, ≥70%) were purchased from Merck KGaA, Darmstadt, Germany and BASF Co., Ltd, Beijing, China, respectively. A laboratory-grade RO-ultrapure water system (resistance >18.3 MΩ cm) supplied deionized (DI) water for the experiments.

**Table 1.** Composition of the industrially Li-containing wastewater.

Parameters	Units	Mean ± SD *
Na^+	mg/L	102.6 ± 2.5
Li^+	mg/L	1252.8 ± 13.5
Ni^{2+}	mg/L	0.0075 ± 0.0002
K^+	mg/L	0.575 ± 0.03
Mg^{2+}	mg/L	0.009 ± 0.0002
Conductivity	mS/cm	21.4 ± 3.2
pH	-	8.51 ± 0.2

* SD: standard deviation of triplicate measurements.

2.2. Fluidized Bed Homogeneous Granulation (FBHo-G) Experiments

Figure 1 presents the schematic diagram of the Li_3PO_4 recovery process using the FBHo-G. The setup consisted of a Pyrex-glass fluidized bed reactor, in which the upper part had an inner diameter of 6.0 cm and a height of 25 cm, and the lower part had an inner diameter of 2 cm and a height of 80 cm. The volume of the reactor was 550 mL. The operational temperatures (from 15–75 °C) were controlled by an electric heater. The flows of real lithium wastewater (Q_{Li}), precipitant (Q_P) and recirculation (Q_R) were fed from the bottom of the reactor using peristaltic pumps (Masterflex® Peristaltic, Fisher Scientific, Leicestershire, England). NaOH and HNO_3 were used to adjust the pH of the Li^+ and PO_4^{3-} solutions. It was important to ensure that nucleation and crystal growth rates were within the correct range so that the formed small fine crystals settled as slurry or suspended in the reactor. At certain intervals, two samples (10 mL each) were collected at the recirculation section to investigate the total and dissolved effluent Li^+ concentrations. The first samples were not unfiltered but digested right away with HNO_3. At the same time,

the second samples were filtered with 0.22 μm micro syringe filters and then preserved with HNO$_3$. A typical experimental run lasted for at least 5 HRTs. The experimental parameters are summarized in Table S1.
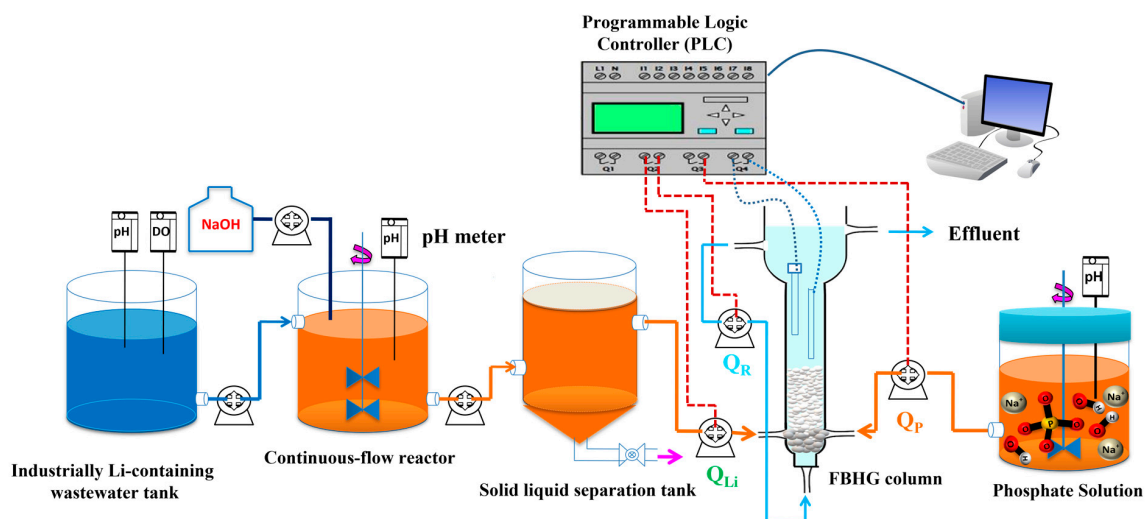
Figure 1. Schematic diagram of lithium recovery using the FBHo-G reactor.

The total removal (TR%, Equation (1)) and granulation ratio (GR%, Equation (2)), which described the total and granular lithium precipitation efficiencies, respectively, were calculated to evaluate the performance of the FBHo-G process [45]. The surface loading of Li$^+$ ions per cross-sectional area was calculated from Equation (3) [53].

$$\text{TR} = \left(1 - \frac{[\text{Li}]_s \times Q_t}{[\text{Li}]_{in} \times Q_{Li}}\right) \times 100\% \tag{1}$$

$$\text{GR} = \left(1 - \frac{[\text{Li}]_t \times Q_t}{[\text{Li}]_{in} \times Q_{Li}}\right) \times 100\% \tag{2}$$

$$\text{SL}_{in} = \frac{[\text{Li}]_{in} \times Q_t}{A_{FBR}} \tag{3}$$

where $[\text{Li}]_{in}$, $[\text{Li}]_s$, and $[\text{Li}]_t$ are the initial, soluble, and total Li$^+$ concentrations (mg-Li/L), respectively; Q_t and Q_{Li} are the total and Li$^+$ influx rates (mL/min), respectively; A_{FBR} is the cross-sectional area of the lower part of the reactor (m^2). The granular pellets were withdrawn from the bottom, dried at 60 °C for 24 h in an oven, and measured for purity and size (details provided in the Supporting Information-SI, Text S1).

2.3. Instrumental Analysis

The pH was measured with a pH/mV meter (8601 AZ pH Meter, AZ Instrument Corp., Taichung, Taiwan). The cationic and anionic concentrations were measured using an Inductively Coupled Plasma Optical Emission Spectrometer (ICP-OES, ULTIMA 2000, HORIDA Ltd., Shimadzu, Japan) and a Flow Injection Analyzer (FIA, Lachat Instruments, 5600 Lindbergh Drive, Loveland, CO, USA), respectively. The instrument detection limits (IDLs) of Li$^+$ and PO$_4^{3-}$ were 0.03 and 0.002 ppm, respectively [47]. The morphology and surface composition of the pellet products were studied using a Scanning Electron Microscopy (SEM, JOEL JXA-840, HITACHI S4100, Chiyoda, Tokyo, Japan) at 10 kV and 7 mA and an Energy Dispersive X-ray Spectroscopy (EDX, LINKS AN10000/85S, Chiyoda, Tokyo, Japan), respectively. Since Li$^+$ ion could not be analyzed using conventional EDX detectors [54], the presence of phosphorus, carbon, and oxygen was used to identify the Li$_3$PO$_4$ phase. The surface functional groups of the pellets were determined using Fourier-Transform Infrared Spectroscopy (FT-IR, Thermo Fisher Scientific, Nicolet 6700, Waltham,

MA, USA) within the range of 4000–400 cm^{-1} at room temperature with the samples embedded in potassium bromide pellets. The crystal phase of the pellets was analyzed using an X-ray Diffractometer (XRD, DX III, Rigaku Co., Ltd, Tokyo, Japan), which operated at 2θ angles $10° < 2θ < 90°$ (scan step: 0.06°; step size 10°/s).

3. Results and Discussion

3.1. FBHo-G Recovery of Li

3.1.1. Effects of Temperature

Figure 2a shows that the reaction temperature (15–90 °C) significantly affected the total Li recovery. At 15 °C, the final Li recovery was only 20%, while it increased to up to 90% at higher temperatures (30–90 °C). In terms of thermal dynamic, Li recovery reached up to 90% after 1 min at 75 °C. The activation energy of Li_3PO_4 precipitation was 366.1 kJ/mol, indicating that such precipitation was endothermic and, thus, the increase in temperature should provide a good support for Li recovery (Figure S1). In addition, at 90 °C, the recovery decreased slightly, to 88.5% after 5 min, and remained constant through the whole experiment. The reason is due to excessive high temperatures (>90 °C), which increase the dissolution rate of the precipitated Li_3PO_4 [50].
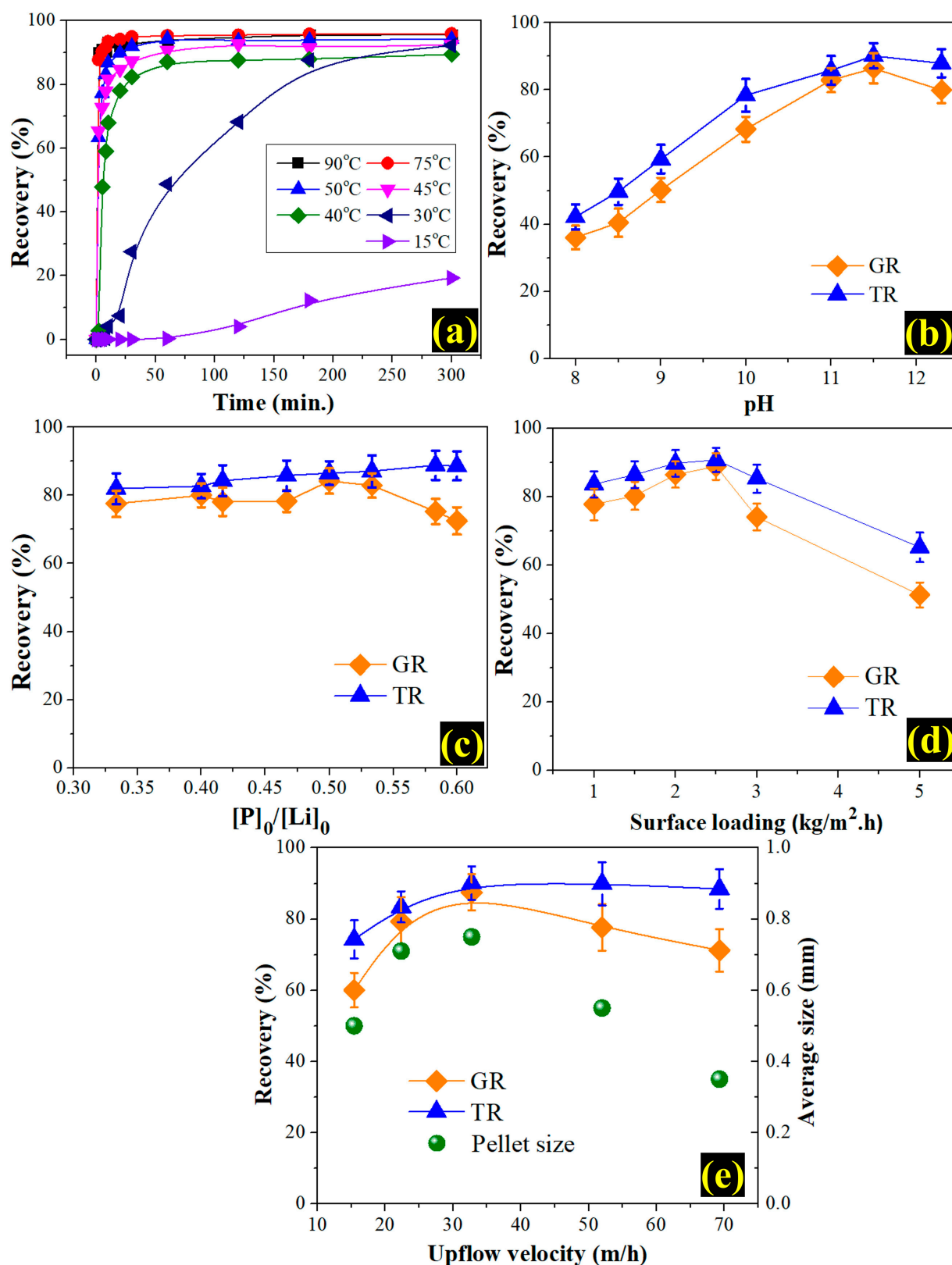
3.1.2. Effects of Effluent pH

Figure 2b shows the effects of effluent pH on Li recovery. Overall, as pH increased from 8.0 to 11.5, the system was supersaturated, and nucleation and crystal growth were promoted (both TR% and GR% increased from ~40% to 90%). The increase in pH facilitated the supersaturation, allowing more Li^+ and PO_4^{3-} ions to interact and form discrete nuclei, which then agglomerated and grew into granules. From our observation, a higher amount of Li^+ at high pH led to stronger interaction among nuclei particles, and more compact and smoother granules. The highest recovery efficiency (TR 90.2% and GR 88.2%) was obtained at pH 11.5.

The critical point of pH is 12.5, at which TR% and GR% started decreasing (e.g., 6%) or remained stable. At high pH conditions, the formation of fines became predominant, resulting in a rapid and spontaneous nucleation, thus compromising GR. The increase of pH from 11.5 to 12.5 may increase the dissolution of Li_3PO_4, making the precipitation and dissolution of this compound in equilibrium and, thus, ceasing the rise of Li recovery. In contrast, when the pH was over 12.0, the PO_4^{3-} ions could combine with H^+ to form HPO_4^{2-}, and the reduction of H^+ ions should be beneficial to the precipitation of Li_3PO_4, increasing TR slightly (by 0.7%); this could be due to LiOH formation, which compromises crystallization, and the production of lightweight sludge (as the precipitation of LiOH is now favored, and most of it would flow out of the reactor in the effluent). The formation of Li products (summarized in Text S2) depended strongly on the pH of the solution (Figure S2). As pH increased, the final concentration of PO_4^{3-} increased, and in contrast, that of Li^+ decreased gradually, indicating that high pH values should facilitate lithium phosphate precipitation, suggesting that the optimum pH window for the crystallization of Li^+ (as Li_3PO_4) was between 11.0 and 11.5.0.

3.1.3. Effects of $[P]_0/[Li]_0$ Molar Ratios

Effects of $[P]_0/[Li]_0$ molar ratios (0.33–0.6) on the Li recovery are shown in Figure 2c. When the $[P]_0/[Li]_0$ ratios increased from 0.33 to 0.475, the TR% and GR% remained relatively stable at approximately 83% and 78%, respectively. When the ratios further increased to 0.5, TR% increased to 87%, and GR% reached its highest at 84.2%. After that, when $[P]_0/[Li]_0$ increased to 0.6, while the TR% stayed at around 88%, GR% dropped by around 10%. The increase in the molar ratio of $[P]_0/[Li]_0$ was able to improve the supersaturation as more PO_4^{3-} ions were released, accelerating the reaction described in Equation (7) and, thus, increasing Li recovery. However, after increasing to a certain value, high $[P]_0/[Li]_0$ may increase the impurity (i.e., $NaKPO_4$) content, which could be entrapped in the precipitated Li_3PO_4, reducing its purity.

Figure 2. Effects of (**a**) temperature, (**b**) effluent pH, (**c**) molar ratios of $[P]_0/[Li]_0$, and (**d**) surface loadings on Li recovery in FBHo-G reactor; and (**e**) effects of U and pellet size distribution. General experimental conditions for all the tests (excluding the investigated parameters): 75 °C, pH 11.5, $[P]_0/[Li]_0$ 0.5, $[Li^+]_{in}$ = 1252.8 mg/L, HRT 30 min. Error bars show the standard deviation for duplicate experiments.

3.1.4. Effects of Surface Loadings

The effects of surface loadings on Li recovery are shown in Figure 2d. The surface loadings were controlled by varying the influx rates of the Li^+ and $PO_4{}^{3-}$. Basically, higher surface loadings mean lower HRT, and vice versa. The increase in the $[Li^+]_{in}$ loading from 1.0 to 2.5 kg/m^{-2} h resulted in both the TR% and the GR% remaining at ~90%. However, as the $[Li^+]_{in}$ loading increased to 3.0 kg/m^{-2} h, the TR% and the GR% both reduced to ~80%. This was due to the accumulation of more fines as a result of faster influx rates. The nucleation of fines in the upper part of the reactor occurred quickly and resulted in less time for crystal growth [45]. As the $[Li^+]_{in}$ loading increased to 5.0, the TR% and the GR% decreased to ~70% and 60%, respectively. The high supersaturation at high surface loadings should stimulate the precipitation of Li_3PO_4. However, as surface loadings increased, HRT was shortened, reducing the collision frequency of small nuclei, quickly draining small particles out of the reactor, and thus, reducing the GR% [46].

3.1.5. Effects of Up-Flow Velocities (U_{mf})

The effects of U_{mf} on Li recovery are displayed in Figure 2e. When the U_{mf} increased from 15.4 to 32.7 m/h, the TR% and the GR% increased from ~75% and 60% to ~90%, respectively. However, as the U_{mf} increased further, to 69.3 m/h, the TR% decreased slightly, to around 88%, and the GR% quickly decreased, to about 80%. When the U_{mf} was between 15.4 and 32.7 m/h, the new nuclei intrinsically formed agglomerates, which then became bigger pellets, improving the TR% and the GR% [55]. The transformation from the metastable phase to the particle underwent a recrystallization process at a low supersaturation and a long HRT [39]. Accordingly, the average pellet size grew from 0.5–0.7 mm. Yet, a higher U_{mf} (than 32.7 m/h) lowered the HRT, reducing the production of Li particles and causing the aggregation and entrapment of liquid inside the granules [46]. At 69.3 m/h, the pellet size dropped to 0.42 mm. This phenomenon could be attributed to the breakage of the newly formed particles under intensive turbulence, which produced a significant number of new primary nuclei.

In order to effectively establish the fluidization, the up-flow stream should surpass a minimum fluid velocity at which the gravitational force on the particles is maintained at a fluidized state [49,56]. This hydrodynamic characteristic can be determined using the Ergun equation [Equation (4)], which helps identify the up-flow velocity (U_{mf} in m/s) for instigating bed fluidization.

$$\frac{\rho_f\left(\rho_s - \rho_f\right)gd_p^3}{\mu^2} = \frac{150\left(1 - \varepsilon_{mf}\right)}{\phi_s^2\varepsilon_{mf}^3}\left(\frac{d_pU_{mf}\rho_g}{\mu}\right) + \frac{1.75}{\phi_s\varepsilon_{mf}^3}\left(\frac{U_{mf}d_p\rho_f}{\mu}\right)^2 \tag{4}$$

The Reynolds number was calculated as follows:

$$Re = \frac{U_{mf} \times d\rho \times \rho_f}{\mu} \tag{5}$$

$$\text{If, Re} > 1000,\ U_{mf} = \frac{\phi_s^2 d_p^2}{150}\cdot\frac{\rho_s - \rho_f}{\mu}g\left(\frac{\varepsilon_{mf}^3}{1 - \varepsilon_{mf}}\right) \tag{6}$$

$$\text{Re} < 20,\ U_{mf}^2 = \frac{\Phi^2 D_p^2\varepsilon_{mf}^3\left(\rho_s - \rho_f\right)g}{150\mu\left(1 - \varepsilon_{mf}\right)} \tag{7}$$

where ρ_f is the density of the fluid (0.9999 g/cm^3), g is the gravitational acceleration constant (980 cm/s^2), Φ_s is the sphericity of particles (0.67), and μ is the viscosity of the fluid (8.94 × 10^{-3} g/cm). With a solid density (ρ_s) of 1.80 g/cm^3 [57], an average diameter (d_p) 0.055 cm, and a void fraction (ε_{mf}) is 0.490, the U_{mf} of the Li_3PO_4 precipitation was 5.3 m/h. A fluctuation of U_f between 15.4 and 32.7 m/h, which was 2.9–6.2 times the

U_{mf}, should be maintained to help maximize the Li_3PO_4 granulation, since it ensured the complete bed fluidization.

3.2. Characteristics of FBHo-G Pellets

Figure 3a,b show the SEM images of FBHo-G pellets collected under the optimal conditions (determined based on the above experiments). The pellets were of a spherical shape with a smooth surface and a diameter 0.2–0.6 mm. The formed pellets had hard structure and were difficult to be broken, which was due to the compact agglomeration of particles during granulation. Figure 3c presents the FTIR spectrum of the lithium granules. Distinct PO_4^{3-} related absorption peaks were observed at 579 cm^{-1} [58] and 1050 cm^{-1} [58], and the H–O–H bond at 1650 cm^{-1} band evidenced the presence of water and phosphate groups in solid form, which may refer to $Li_3PO_4 \cdot xH_2O$ formation. The band at 3400 cm^{-1} indicates O–H stretching vibration, confirming the deposition of hydroxide species of Li onto the solid surface [59]. The strong XRD peaks (Figure 3d) of the pellets confirmed their crystallinity. The crystal phase was determined for Li_3O_4P (JCPDS card no.01-71-1528) with 2θ peaks at 16.7°, 22.3°, 23.4°, 25.1°, 29.2°, 34.2°, 38.8°, 51.1°, and 63.3° for facets of (010), (110), (101), (011), (111), (210), (002), (212), and (230), respectively [60]. From the EDX results in Figure 3e, the main surface composition of the pellets included C (14.96%), O (56.86%), and P (15.93%), suggesting that phosphate existed in the precipitated pellets. Since Li^+ ion could not be analyzed using conventional EDX detectors, ICP was employed to further analyze the composition of the pellets (Table S2). The major impurities of the pellets were K (<0.005 wt%) and Na (~3 wt%), which could be due to the co-precipitation of $LiKPO_4$ and the pH adjustment using NaOH, respectively. Also, the water content of the pellets was below 5%, which is significantly lower than that of the sludge produced by the chemical precipitation recovery method, indicating that the pellets could be used as a raw materials to resynthesize cathode materials [61].
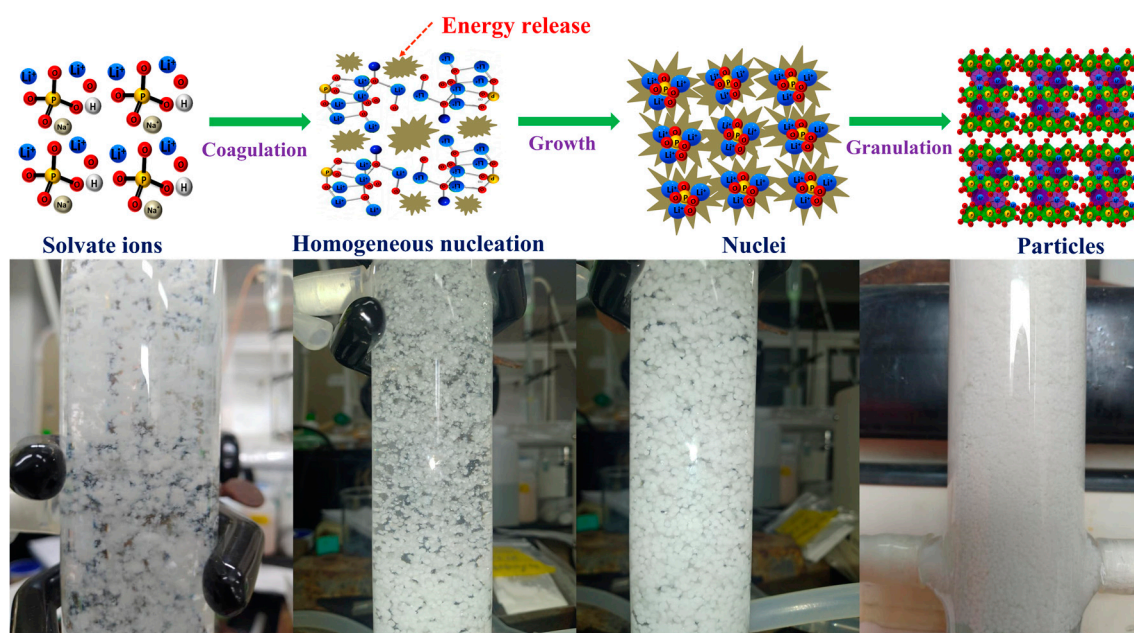
3.3. Recovery Mechanisms of FBHo-G Process

Based on the above theoretical and experimental results, the mechanisms of the Li_3PO_4 granulation process were proposed and summarized in Figure 4. At first, localized hot spots were formed with increasing numbers of solvated Li^+, PO_4^{3-}, and $LiOH^-$ ions. Then, the rates of chemical reactions and the dissolution of sodium hydroxide increased, while the solubility of lithium and that of phosphate decreased [62]. The combination of lithium and phosphate ions occurred more frequently, and the Li_3PO_4 precipitation could be found at the bottom of the fluidized bed [63]. Due to the hydraulic load motion kinetics, the nuclei continued to grow by colliding with each other within the up-flow stream. The $Li_3PO_4 \cdot xH_2O$ crystals (or fluidized particles) could be visualized gradually [63]. In the Li_3PO_4 phase, the Li^+ ions bound to oxygen atoms, which connected with phosphorus atoms through corner-sharing [64]. The orthorhombic Li_3PO_4 crystallized in a rod-like shape over the primary crystals [65]. The grown particles became dense and sank to the middle region, where they clustered and entrapped liquid. The crystals spread and deposited on the nuclei's surface, and the nuclei then gradually grew into precipitated particles. The hydraulic turbulence allowed the compaction of the aggregates at the upper part of the reactor. The compact aggregates continued to collide, fragment, and compress to form bigger clusters [54]. The homogenous granulation reduced the Li_3PO_4 supersaturation at the solid–liquid interface, and the spontaneous nucleation and granular growth co-occurred in the metastable zone [49]. The aggregation and the breakup of particles gradually reached a steady state, resulting in the formation of $Li_3PO_4 \cdot xH_2O$ granules. Finally, the granules then precipitated out via solid–liquid bridging [64].
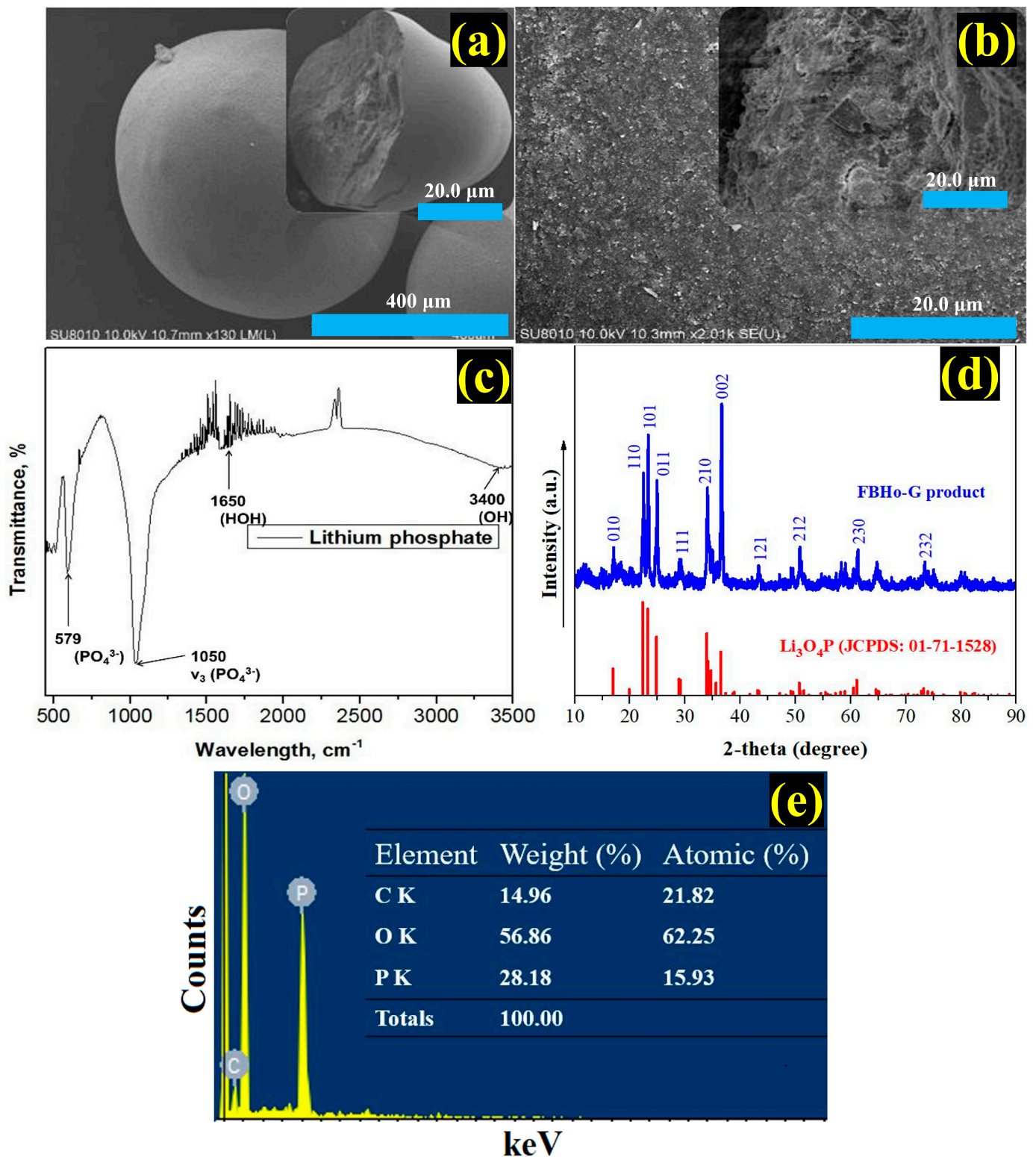
Figure 3. SEM images of (**a**) Li₃PO₄ particles (130× magnification, scale bar 400 μm) and inset (120× magnification, scale bar 400 μm) and (**b**) particle surface (2000× magnification, scale bar 20 μm) and inset of pellet's interior surface (2000× magnification, scale bar 50 μm); (**c**) FTIR pattern, (**d**) XRD spectra, and (**e**) EDX data of pellet products. Experimental conditions: 75 °C, pH 11.5, $[P]_0/[Li]_0$ 0.5, U 37.3 m/h, $[Li]_{in}$ =1252.8 mg/L, HRT 30 min.

Figure 4. Summary of Li recovery mechanisms by FBHo-G process.

3.4. Economic Analysis

Economic feasibility determines the prospect of a technology to be applied at an industrial scale. It is noted that, to curtail several uncertainties, other internal and external net benefits, such as a reduction in sludge management cost, pipe cleaning and maintenance cost, marketing management, and so forth, were set to zero. Therefore, here, a brief economic analysis of using the FBHo-G for lithium recovery was conducted (Table 2). The input chemicals (Na_2HPO_4 and $NaOH$) and the output number of pellets were calculated based on the ideal mass balance of the recovery of lithium phosphate. The energy cost was calculated based on a 120 h FBHo-G run. From the industrially Li-containing wastewater used in this study, a m^3 of the wastewater contained up to ~0.205 kg of Li [66]. With a recovery rate of ~90%, the FBHo-G process could recover up to 0.1845 kg of lithium per m^3 of Li-containing wastewater. The operation should require the use of 12.5 kg of Na_2HPO_4 and 3.5 kg of NaOH. Not having to treat the Li-containing wastewater may help save up to USD 33.92. The gained profit for selling lithium phosphate pellets (portrayed in Figure S3) was briefly estimated to be USD 47.960 (per m^3 of Li-containing wastewater). The Li_3PO_4 pellets had a low water content (<5%), meaning that they could be used directly as chemical reagents and a raw materials for industrial applications (e.g., cathode synthesis) [5]. The market price of Li_3PO_4 is exceptionally high, making Li recovery a worthwhile attempt. It should be noted, however, that this is only a brief economic analysis, where costs of labor, equipment, facility, etc. are not included. Future detailed economic and life cycle assessments are highly welcomed.

Table 2. Economic analysis of lithium recovery using the fluidized bed homogeneous granulation process.

Parameters	Amount Used	Electricity Cost (USD/kWh) *	Chemical Cost (USD/kg) **	Product's Market Price (USD/kg) ***	Cost (USD)
1. Operational cost					**25.971**
- NaOH (China, purity: 99%)	3.5		0.290		1.015
- Na_2HPO_4 (China, purity: 99%)	12.5		1.886		23.57
- Energy for influent feeding pump	4.5	0.132			0.594

Table 2. *Cont.*

Parameters	Amount Used	Electricity Cost (USD/kWh) *	Chemical Cost (USD/kg) **	Product's Market Price (USD/kg) ***	Cost (USD)
- Energy for NaOH feeding pump	2.5	0.132			0.33
- Energy for pellet drying	3.5	0.132			0.462
2. Revenue					**47.960**
Harvested Li_3PO_4 pellets	0.1845			259.95	47.960
Average Li recovery (%)	88.9				
3. Profit margin = (2) — (1)					**21.989**

Remark: data were estimated based on one m^3 of Li-containing wastewater. The calculations were mostly based on the lab-scale FBHo-G process. Costs of labor, equipment, and facility were not included. (*) Taiwan's electricity cost from Taiwan Power Company (https://www.taipower.com.tw/, accessed on 25 December 2023). (**) Price of chemical derived from commercial webpage. (***) Price of Li_3PO_4 powder derived from MSE Supplies LLC (https://www.msesupplies.com/, accessed on 2 February 2024)".

4. Conclusions

In this study, for the first time, fluidized bed homogeneous granulation technology was used for the recovery of Li in the form of Li_3PO_4. The actual Li-rich industrial effluent was employed, and the recovered product was in the form of Li_3PO_4 pellets. The following results were obtained:

- In terms of thermal dynamic, Li recovery reached up to 90% after 1 min at 75 °C. The activation energy of Li_3PO_4 precipitation was 366.1 kJ/mol, indicating that such precipitation was endothermic and, thus, the increase in temperature should provide a good support for Li recovery.
- Under the optimum pH of 11.5, temperature of 75 °C, cross-sectional surface loading of 2.5 kg/m^2·h, up-flow velocity of 35.7 m/h, and $[P]_0/[Li]_0$ of 0.5, the total Li removal in the FBHG reactor reached about 90%, which corresponds to the residual Li ion concentration of 80 mg/L. The crystallization ratio of Li pellets reached up to about 88.2%.
- The XRD, EDX, and FT-IR analysis indicated that Li^+ ions bound to oxygen atoms, which connected with phosphorus atoms through corner-sharing. The orthorhombic Li_3PO_4 crystallized in a rod-like shape over the primary crystals. The grown particles became dense and sank to the middle region, where they clustered and entrapped liquid. Finally, the granules then precipitated out via solid-liquid bridging.
- The material characterization of the recovery pellet products showed that they were highly crystallized Li_3PO_4, with a purity of ~88.9%. Their high purity enables them to be further directly reused as raw materials in a wide range of industrial applications (e.g., in the synthesis of cathode materials).
- Our calculation shows that the FBHo-G process could recover up to 0.1845 kg of lithium per cubic meter of Li-containing wastewater, at a recovery rate of ~90%. Moreover, the results obtained from the cost–benefit analysis highlighted that the FBHG process had economic viability, with a net profit of USD 22/m^3 Li treated and an estimated production cost of USD 26/kg Li removed. In all, fluidized-bed homogeneous granulation, a seedless one-step recovery process, opens a promising pathway toward a green and sustainable recycling industry for the recovery and application of the resource-limited lithium element from nonconventional water sources.

Supplementary Materials: The following supporting information can be downloaded at: https://www.mdpi.com/article/10.3390/min14060603/s1, Figure S1: Arrhenius plot calculated for precipitating lithium phosphate at different temperatures [data were fitted with the Arrhenius equation: $\ln k = -E\_a/RT + \ln A$, where R is the energy gas constant (J/(mol·K)), A the pre-exponential factor, Ea the activation energy (kJ/mol), and T (K) the temperature; Figure S2: The Log[Me]$_T$-pH diagram of species existing in the FBHo-G reactor; Figure S3: Photo of lithium phosphate crystal products and

their different particle sizes; Table S1: Experimental parameters of the FBHo-G process; Table S2: ICP elemental analysis of FBHo-G pellets; Text S1: Analysis of purity of the pellet products and pellet size distribution; Text S2: Thermodynamic calculations of reaction products in the FBHo-G reactor.

References

1. Niu, C.; Liu, D.; Lochala, J.A.; Anderson, C.S.; Cao, X.; Gross, M.E.; Xu, W.; Zhang, J.-G.; Whittingham, M.S.; Xiao, J.; et al. Balancing interfacial reactions to achieve long cycle life in high-energy lithium metal batteries. *Nat. Energy* **2021**, *6*, 723–732. [CrossRef]
2. Swain, B. Recovery and recycling of lithium: A review. *Sep. Purif. Technol.* **2017**, *172*, 388–403. [CrossRef]
3. Hua, X.; Eggeman, A.S.; Castillo-Martínez, E.; Robert, R.; Geddes, H.S.; Lu, Z.; Pickard, C.J.; Meng, W.; Wiaderek, K.M.; Pereira, N.; et al. Revisiting metal fluorides as lithium-ion battery cathodes. *Nat. Mater.* **2021**, *20*, 841–850. [CrossRef] [PubMed]
4. Zhang, K.; An, Y.; Wei, C.; Qian, Y.; Zhang, Y.; Feng, J. High-safety and dendrite-free lithium metal batteries enabled by building a stable interface in a nonflammable medium-concentration phosphate electrolyte. *ACS Appl. Mater. Interfaces* **2021**, *13*, 50869–50877. [CrossRef] [PubMed]
5. Weiss, M.; Ruess, R.; Kasnatscheew, J.; Levartovsky, Y.; Levy, N.R.; Minnmann, P.; Stolz, L.; Waldmann, T.; Wohlfahrt-Mehrens, M.; Aurbach, D.; et al. Fast Charging of Lithium-Ion Batteries: A Review of Materials Aspects. *Adv. Energy Mater.* **2021**, *11*, 2101126. [CrossRef]
6. Ma, L.; Lv, Y.; Wu, J.; Chen, Y.; Jin, Z. Recent Advances in Emerging Non-Lithium Metal–Sulfur Batteries: A Review. *Adv. Energy Mater.* **2021**, *11*, 2100770. [CrossRef]
7. Liu, J.; Cao, D.; Yao, H.; Liu, D.; Zhang, X.; Zhang, Q.; Chen, L.; Wu, S.; Sun, Y.; He, D. Hexagonal Boron Nitride-Coated Polyimide Ion Track Etched Separator with Enhanced Thermal Conductivity and High-Temperature Stability for Lithium-Ion Batteries. *ACS Appl. Energy Mater.* **2022**, *5*, 8639–8649. [CrossRef]
8. Jiang, L.; Liang, C.; Li, H.; Wang, Q.; Sun, J. Safer triethyl-phosphate-based electrolyte enables nonflammable and high-temperature endurance for a lithium ion battery. *ACS Appl. Energy Mater.* **2020**, *3*, 1719–1729. [CrossRef]
9. Wang, J.; Li, S.; Zhang, J.; Song, L.; Dong, H.; Zhang, N.; Wang, P.; Zhao, D.; Zhang, L.; Cui, X. Improving Toleration of Volume Expansion of Silicon-Based Anode by Constructing a Flexible Solid-Electrolyte Interface Film via Lithium Difluoro (bisoxalato) Phosphate Electrolyte Additive. *ACS Sustain. Chem. Eng.* **2022**, *10*, 15199–15210. [CrossRef]
10. LaCoste, J.D.; Zakutayev, A.; Fei, L. A review on lithium phosphorus oxynitride. *J. Phys. Chem. C* **2021**, *125*, 3651–3667. [CrossRef]
11. Masquelier, C.; Croguennec, L. Polyanionic (phosphates, silicates, sulfates) frameworks as electrode materials for rechargeable Li (or Na) batteries. *Chem. Rev.* **2013**, *113*, 6552–6591. [CrossRef] [PubMed]
12. Auvergniot, J.; Cassel, A.; Ledeuil, J.-B.; Viallet, V.; Seznec, V.; Dedryvère, R. Interface stability of argyrodite Li_6PS_5Cl toward $LiCoO_2$, $LiNi_{1/3}Co_{1/3}Mn_{1/3}O_2$, and $LiMn_2O_4$ in bulk all-solid-state batteries. *Chem. Mater.* **2017**, *29*, 3883–3890. [CrossRef]
13. Greim, P.; Solomon, A.A.; Breyer, C. Assessment of lithium criticality in the global energy transition and addressing policy gaps in transportation. *Nat. Commun.* **2020**, *11*, 4570. [CrossRef] [PubMed]
14. Jacoby, M. It's time to recycle lithium-ion batteries. *CEN Glob. Enterp.* **2019**, *97*, 29–32. [CrossRef]
15. Garole, D.J.; Hossain, R.; Garole, V.J.; Sahajwalla, V.; Nerkar, J.; Dubal, D.P. Recycle, recover and repurpose strategy of Spent Li-ion Batteries and catalysts: Current status and future opportunities. *ChemSusChem* **2020**, *13*, 3079–3100. [CrossRef] [PubMed]
16. Ding, Y.; Nhung, N.T.H.; An, J.; Chen, H.; Liao, L.; He, C.; Wang, X.; Fujita, T. Manganese-Titanium Mixed Ion Sieves for the Selective Adsorption of Lithium Ions from an Artificial Salt Lake Brine. *Materials* **2023**, *16*, 4190. [CrossRef] [PubMed]
17. Chen, H.; Liao, L.; Ding, Y.; He, C.; Dodbiba, G.; Wang, X.; Fujita, T. Feasible route for the regeneration of cathode materials from spent lithium-ion batteries via reduction leaching and in-site precipitation. *J. Power Sources* **2024**, *598*, 234155. [CrossRef]

18. Liu, T.; Gao, X.; Mofrad, A.Z.; Kudo, S.; Asano, S.; Hayashi, J.-i. Leaching Char with Acidic Aqueous Phase from Biomass Pyrolysis: Removal of Alkali and Alkaline-Earth Metallic Species and Uptakes of Water-Soluble Organics. *Energy Fuels* **2021**, *35*, 12237–12251. [CrossRef]

19. Su, H.; Li, Z.; Zhang, J.; Liu, W.; Zhu, Z.; Wang, L.; Qi, T. Combining selective extraction and easy stripping of lithium using a ternary synergistic solvent extraction system through regulation of Fe^{3+} coordination. *ACS Sustain. Chem. Eng.* **2020**, *8*, 1971–1979. [CrossRef]

20. Chen, W.; Li, X.; Chen, L.; Zhou, G.; Lu, Q.; Huang, Y.; Chao, Y.; Zhu, W. Tailoring hydrophobic deep eutectic solvent for selective lithium recovery from the mother liquor of Li_2CO_3. *Chem. Eng. J.* **2021**, *420*, 127648. [CrossRef]

21. Vu, C.T.; Wu, T. Engineered multifunctional sand for enhanced removal of stormwater runoff contaminants in fixed-bed column systems. *Chemosphere* **2019**, *224*, 852–861. [CrossRef] [PubMed]

22. Wahib, S.A.; Da'na, D.A.; Zaouri, N.; Hijji, Y.M.; Al-Ghouti, M.A. Adsorption and recovery of lithium ions from groundwater using date pits impregnated with cellulose nanocrystals and ionic liquid. *J. Hazard. Mater.* **2022**, *421*, 126657. [CrossRef] [PubMed]

23. Chen, J.; Lin, S.; Yu, J. Quantitative effects of Fe_3O_4 nanoparticle content on Li+ adsorption and magnetic recovery performances of magnetic lithium-aluminum layered double hydroxides in ultrahigh Mg/Li ratio brines. *J. Hazard. Mater.* **2020**, *388*, 122101. [CrossRef] [PubMed]

24. Lai, X.; Yuan, Y.; Chen, Z.; Peng, J.; Sun, H.; Zhong, H. Adsorption–Desorption Properties of Granular EP/HMO Composite and Its Application in Lithium Recovery from Brine. *Ind. Eng. Chem. Res.* **2020**, *59*, 7913–7925. [CrossRef]

25. Vu, C.T.; Wu, T. Magnetic porous NiLa-Layered double oxides (LDOs) with improved phosphate adsorption and antibacterial activity for treatment of secondary effluent. *Water Res.* **2020**, *175*, 115679. [CrossRef] [PubMed]

26. Chen, X.; Ruan, X.; Kentish, S.E.; Li, G.K.; Xu, T.; Chen, G.Q. Production of Lithium Hydroxide by Electrodialysis with Bipolar Membranes. *Sep. Purif. Technol.* **2021**, *274*, 119026. [CrossRef]

27. Zhao, Z.; Liu, G.; Jia, H.; He, L. Sandwiched liquid-membrane electrodialysis: Lithium selective recovery from salt lake brines with high Mg/Li ratio. *J. Membr. Sci.* **2020**, *596*, 117685. [CrossRef]

28. Wang, L.; Rehman, D.; Sun, P.-F.; Deshmukh, A.; Zhang, L.; Han, Q.; Yang, Z.; Wang, Z.; Park, H.-D.; Lienhard, J.H. Novel Positively Charged Metal-Coordinated Nanofiltration Membrane for Lithium Recovery. *ACS Appl. Mater. Interfaces* **2021**, *13*, 16906–16915. [CrossRef] [PubMed]

29. Peng, H.; Zhao, Q. A Nano-Heterogeneous Membrane for Efficient Separation of Lithium from High Magnesium/Lithium Ratio Brine. *Adv. Funct. Mater.* **2021**, *31*, 2009430. [CrossRef]

30. Zhang, Y.; Wang, W.; Hu, J.; Zhang, T.; Xu, S. Stepwise Recovery of Valuable Metals from Spent Lithium Ion Batteries by Controllable Reduction and Selective Leaching and Precipitation. *ACS Sustain. Chem. Eng.* **2020**, *8*, 15496–15506. [CrossRef]

31. Gu, S.; Zhang, L.; Fu, B.; Wang, X.; Ahn, J.W. Feasible route for the recovery of strategic metals from mixed lithium-ion batteries cathode materials by precipitation and carbonation. *Chem. Eng. J.* **2021**, *420*, 127561. [CrossRef]

32. Hashemi, R.; Nassar, N.N.; Almao, P.P. Nanoparticle technology for heavy oil in-situ upgrading and recovery enhancement: Opportunities and challenges. *Appl. Energy* **2014**, *133*, 374–387. [CrossRef]

33. Luo, X.; Guo, B.; Luo, J.; Deng, F.; Zhang, S.; Luo, S.; Crittenden, J. Recovery of lithium from wastewater using development of Li ion-imprinted polymers. *ACS Sustain. Chem. Eng.* **2015**, *3*, 460–467. [CrossRef]

34. An, J.W.; Kang, D.J.; Tran, K.T.; Kim, M.J.; Lim, T.; Tran, T. Recovery of lithium from Uyuni salar brine. *Hydrometallurgy* **2012**, *117*, 64–70. [CrossRef]

35. Battaglia, G.; Berkemeyer, L.; Cipollina, A.; Cortina, J.L.; Fernandez de Labastida, M.; Lopez Rodriguez, J.; Winter, D. Recovery of Lithium Carbonate from Dilute Li-Rich Brine via Homogenous and Heterogeneous Precipitation. *Ind. Eng. Chem. Res.* **2022**, *61*, 13589–13602. [CrossRef]

36. Meunier, N.; Drogui, P.; Montané, C.; Hausler, R.; Mercier, G.; Blais, J.-F. Comparison between electrocoagulation and chemical precipitation for metals removal from acidic soil leachate. *J. Hazard. Mater.* **2006**, *137*, 581–590. [CrossRef]

37. Ahmed, S.F.; Mofijur, M.; Parisa, T.A.; Islam, N.; Kusumo, F.; Inayat, A.; Le, V.G.; Badruddin, I.A.; Khan, T.M.Y.; Ong, H.C. Progress and challenges of contaminate removal from wastewater using microalgae biomass. *Chemosphere* **2022**, *286*, 131656. [CrossRef]

38. Tran, H.T.; Lin, C.; Hoang, H.G.; Bui, X.T.; Le, V.G.; Vu, C.T. Soil washing for the remediation of dioxin-contaminated soil. A review. *J. Hazard. Mater.* **2021**, *421*, 126767. [CrossRef]

39. Lin, J.-Y.; Mahasti, N.N.N.; Huang, Y.-H. Fluidized-bed crystallization of barium perborate for continuous boron removal from concentrated solution: Supersaturation as a master variable. *Sep. Purif. Technol.* **2022**, *278*, 119588. [CrossRef]

40. Lin, J.-Y.; Mahasti, N.N.N.; Huang, Y.-H. Recent advances in adsorption and coagulation for boron removal from wastewater: A comprehensive review. *J. Hazard. Mater.* **2021**, *407*, 124401. [CrossRef]

41. Le, V.-G.; Vu, C.-T.; Shih, Y.-J.; Huang, Y.-H. Highly efficient recovery of ruthenium from integrated circuit (IC) manufacturing wastewater by Al reduction and cementation. *RSC Adv.* **2019**, *9*, 25303–25308. [CrossRef]

42. Lei, Y.; Narsing, S.; Saakes, M.; van der Weijden, R.D.; Buisman, C.J.N. Calcium Carbonate Packed Electrochemical Precipitation Column: New Concept of Phosphate Removal and Recovery. *Environ. Sci. Technol.* **2019**, *53*, 10774–10780. [CrossRef]

43. Lei, Y.; Zhan, Z.; Saakes, M.; van der Weijden, R.D.; Buisman, C.J.N. Electrochemical Recovery of Phosphorus from Acidic Cheese Wastewater: Feasibility, Quality of Products, and Comparison with Chemical Precipitation. *ACS EST Water* **2021**, *1*, 1002–1013. [CrossRef]

44. Le, V.G.; Vo, T.D.H.; Nguyen, B.S.; Vu, C.T.; Shih, Y.J.; Huang, Y.H. Recovery of iron(II) and aluminum(III) from acid mine drainage by sequential selective precipitation and fluidized bed homogeneous crystallization (FBHC). *J. Taiwan Inst. Chem. Eng.* **2020**, *115*, 135–143. [CrossRef]
45. Le, V.-G.; Vu, C.-T.; Shih, Y.-J.; Bui, X.-T.; Liao, C.-H.; Huang, Y.-H. Phosphorus and potassium recovery from human urine using a fluidized bed homogeneous crystallization (FBHC) process. *Chem. Eng. J.* **2020**, *384*, 123282. [CrossRef]
46. Bayon, L.L.E.; Ballesteros, F.C.; Choi, A.E.S.; Garcia-Segura, S.; Lu, M.C. Remediation of cobalt from semiconductor wastewater in the frame of fluidized-bed homogeneous granulation process. *J. Environ. Chem. Eng.* **2021**, *9*, 105936. [CrossRef]
47. Le, V.G.; Vo, D.V.N.; Vu, C.T.; Bui, X.T.; Shih, Y.J.; Huang, Y.H. Applying a Novel Sequential Double-Column Fluidized Bed Crystallization Process to the Recovery of Nitrogen, Phosphorus, and Potassium from Swine Wastewater. *ACS EST Water* **2021**, *1*, 707–718. [CrossRef]
48. Lacson, C.F.Z.; Lu, M.-C.; Huang, Y.-H. Chemical precipitation at extreme fluoride concentration and potential recovery of CaF2 particles by fluidized-bed homogenous crystallization process. *Chem. Eng. J.* **2021**, *415*, 128917. [CrossRef]
49. Chen, C.-S.; Shih, Y.-J.; Huang, Y.-H. Remediation of lead (Pb (II)) wastewater through recovery of lead carbonate in a fluidized-bed homogeneous crystallization (FBHC) system. *Chem. Eng. J.* **2015**, *279*, 120–128. [CrossRef]
50. Liao, P.-L.; Nezha Nunez Mahasti, N.; Huang, Y.-H. The recovery of sulfur as ZnS particles from sulfide-contained wastewater using fluidized bed homogeneous crystallization technology. *Chem. Eng. J.* **2021**, *430*, 133170. [CrossRef]
51. Le, V.G.; Vo, D.V.N.; Tran, H.T.; Duy Dat, N.; Luu, S.D.N.; Rahman, M.M.; Huang, Y.H.; Vu, C.T. Recovery of Magnesium from Industrial Effluent and Its Implication on Carbon Capture and Storage. *ACS Sustain. Chem. Eng.* **2021**, *9*, 6732–6740. [CrossRef]
52. Le, V.-G.; Vo, D.-V.N.; Nguyen, N.-H.; Shih, Y.-J.; Vu, C.-T.; Liao, C.-H.; Huang, Y.-H. Struvite recovery from swine wastewater using fluidized-bed homogeneous granulation process. *J. Environ. Chem. Eng.* **2021**, *9*, 105019. [CrossRef]
53. Abramowitz, M.; Stegun, I.A. *Handbook of Mathematical Functions with Formulas, Graphs, and Mathematical Tables*; US Government Printing Office: Washington, DC, USA, 1972; Volume 55.
54. King, H.E.; Salisbury, A.; Huijsmans, J.; Dzade, N.Y.; Plümper, O. Influence of Inorganic Solution Components on Lithium Carbonate Crystal Growth. *Cryst. Growth Des.* **2019**, *19*, 6994–7006. [CrossRef]
55. Udomkitthaweewat, N.; Anotai, J.; Choi, A.E.S.; Lu, M.C. Removal of zinc based on a screw manufacturing plant wastewater by fluidized-bed homogeneous granulation process. *J. Clean. Prod.* **2019**, *230*, 1276–1286. [CrossRef]
56. Priambodo, R.; Shih, Y.-J.; Huang, Y.-H. Phosphorus recovery as ferrous phosphate (vivianite) from wastewater produced in manufacture of thin film transistor-liquid crystal displays (TFT-LCD) by a fluidized bed crystallizer (FBC). *RSC Adv.* **2017**, *7*, 40819–40828. [CrossRef]
57. Wang, J.; Shen, Z.; Yi, M. Hydraulic Compaction on Electrode to Improve the Volumetric Energy Density of LiFePO$_4$/Graphite Batteries. *Ind. Eng. Chem. Res.* **2019**, *58*, 15407–15415. [CrossRef]
58. Frost, R.L.; López, A.; Theiss, F.L.; Scholz, R.; Souza, L. The molecular structure of the phosphate mineral kidwellite NaFe$_9^{3+}$(PO$_4$)$_6$(OH)$_{11}$·3H$_2$O—A vibrational spectroscopic study. *J. Mol. Struct.* **2014**, *1074*, 429–434. [CrossRef]
59. Ait Salah, A.; Jozwiak, P.; Zaghib, K.; Garbarczyk, J.; Gendron, F.; Mauger, A.; Julien, C.M. FTIR features of lithium-iron phosphates as electrode materials for rechargeable lithium batteries. *Spectrochim. Acta Part A Mol. Biomol. Spectrosc.* **2006**, *65*, 1007–1013. [CrossRef]
60. Li, H.; Xing, S.; Liu, Y.; Li, F.; Guo, H.; Kuang, G. Recovery of Lithium, Iron, and Phosphorus from Spent LiFePO4 Batteries Using Stoichiometric Sulfuric Acid Leaching System. *ACS Sustain. Chem. Eng.* **2017**, *5*, 8017–8024. [CrossRef]
61. Fan, E.; Li, L.; Lin, J.; Wu, J.; Yang, J.; Wu, F.; Chen, R. Low-Temperature Molten-Salt-Assisted Recovery of Valuable Metals from Spent Lithium-Ion Batteries. *ACS Sustain. Chem. Eng.* **2019**, *7*, 16144–16150. [CrossRef]
62. Zhao, C.; Zhang, Y.; Cao, H.; Zheng, X.; Van Gerven, T.; Hu, Y.; Sun, Z. Lithium carbonate recovery from lithium-containing solution by ultrasound assisted precipitation. *Ultrason. Sonochem.* **2019**, *52*, 484–492. [CrossRef]
63. Yang, W.; Zhou, L.; Dai, J.; Zhou, L.; Zhang, M.; Xie, C.; Hao, H.; Hou, B.; Bao, Y.; Yin, Q. Crystallization of Lithium Carbonate from Aqueous Solution: New Insights into Crystal Agglomeration. *Ind. Eng. Chem. Res.* **2019**, *58*, 18448–18455. [CrossRef]
64. Chung, S.-Y.; Kim, Y.-M.; Lee, S.; Oh, S.H.; Kim, J.-G.; Choi, S.-Y.; Kim, Y.-J.; Kang, S.-J.L. Cation Disordering by Rapid Crystal Growth in Olivine-Phosphate Nanocrystals. *Nano Lett.* **2012**, *12*, 3068–3073. [CrossRef]
65. Ayu, N.I.P.; Kartini, E.; Prayogi, L.D.; Faisal, M. Supardi, Crystal structure analysis of Li$_3$PO$_4$ powder prepared by wet chemical reaction and solid-state reaction by using X-ray diffraction (XRD). *Ionics* **2016**, *22*, 1051–1057. [CrossRef]
66. Yang, Y.; Zheng, X.; Cao, H.; Zhao, C.; Lin, X.; Ning, P.; Zhang, Y.; Jin, W.; Sun, Z. A closed-loop process for selective metal recovery from spent lithium iron phosphate batteries through mechanochemical activation. *ACS Sustain. Chem. Eng.* **2017**, *5*, 9972–9980. [CrossRef]